



## Full-field neutron microscopy based on refractive optics

**Leemreize, Hanna; Knudsen, Erik B.; Birk, Jonas O.; Strobl, Markus; Detlefs, Carsten; Poulsen, Henning F.**

*Published in:*  
Journal of Applied Crystallography

*Link to article, DOI:*  
[10.1107/s1600576719012858](https://doi.org/10.1107/s1600576719012858)

*Publication date:*  
2019

*Document Version*  
Peer reviewed version

[Link back to DTU Orbit](#)

*Citation (APA):*  
Leemreize, H., Knudsen, E. B., Birk, J. O., Strobl, M., Detlefs, C., & Poulsen, H. F. (2019). Full-field neutron microscopy based on refractive optics. *Journal of Applied Crystallography*, 52(6).  
<https://doi.org/10.1107/s1600576719012858>

---

### General rights

Copyright and moral rights for the publications made accessible in the public portal are retained by the authors and/or other copyright owners and it is a condition of accessing publications that users recognise and abide by the legal requirements associated with these rights.

- Users may download and print one copy of any publication from the public portal for the purpose of private study or research.
- You may not further distribute the material or use it for any profit-making activity or commercial gain
- You may freely distribute the URL identifying the publication in the public portal

If you believe that this document breaches copyright please contact us providing details, and we will remove access to the work immediately and investigate your claim.

# Full field neutron microscopy based on refractive optics

H. Leemreize,<sup>a,b</sup> E. B. Knudsen,<sup>a</sup> J. O. Birk,<sup>b</sup> M. Strobl,<sup>c</sup> C. Detlefs<sup>d</sup> and H. F. Poulsen<sup>a\*</sup>

<sup>a</sup>Department of Physics, Technical University of Denmark, 2800 Kgs. Lyngby, Denmark, <sup>b</sup>Technological Institute Denmark, <sup>c</sup>Paul Scherrer Institute Switzerland, and <sup>d</sup>European Synchrotron Radiation Facility, 71 avenue des Martyrs, CS40220, 38043 Grenoble Cedex 9, France. Correspondence e-mail: hfpo@fysik.dtu.dk

Placing a compound refractive lens (CRL) as an objective in a neutron beam generates new possibilities for 2D and 3D non-destructive mapping of the structure, strain and magnetic domains within extended objects. **We introduce a condenser set-up that allows to correct for the lateral chromatic aberration. More generally, for full field microscopy the loss in performance caused by the chromatic aberration can be more than offset by introducing arrays of CRLs and exploiting the fact that the field-of-view can be much larger than the physical aperture of the CRL. We comment on the manufacturing of such devices.** The potential use is illustrated by principle comparisons between state-of-the-art instrumentation and suggested approaches for bright field microscopy, SANS microscopy, for grain mapping and for mapping of stresses. We discuss options for depth resolved imaging inspired by confocal light microscopy. Finally, we demonstrate experimentally some of the basic properties of neutron full field imaging for a single CRL.

© 0000 International Union of Crystallography  
Printed in Singapore – all rights reserved

## 1. Introduction

Neutron imaging is a rapidly expanding field (Lehmann, 2015; Kardjilov *et al.*, 2018; Treimer, 2019). The relatively low brilliance of neutron sources implies that imaging experiments typically require the use of a polychromatic beam with a relatively large divergence — in particular this is true for 3D and time resolved studies. With such beams, it is natural to base bright field imaging studies on placing a 2D detector downstream but in close proximity of the sample. This approach enables a large variety of contrast to be explored, including attenuation contrast (Kallmann, 1948; Strobl *et al.*, 2009), phase contrast (Strobl *et al.*, 2008) and more specialised techniques such as spectral imaging (Lehmann *et al.*, 2014), Bragg edge contrast for mapping of stresses (Santisteban *et al.*, 2001) and phases (Peetermans *et al.*, 2014), extinction contrast for mapping of large grains (Cereser *et al.*, 2017), and **some versions of polarized neutron imaging for visualising magnetic field distributions (Sales *et al.*, 2019) and magnetic domains (Kardjilov *et al.*, 2008; Schulz *et al.*, 2010; Strobl *et al.*, 2019; Jorba *et al.*, 2019).**

One basic limitation, though, is that the resolution deteriorates with larger sample volume-detector distances, unless one compromise on the divergence of the incoming beam. This implies a trade-off between spatial resolution and time resolution, and might limit spatial resolution for extended objects and in particular where extensive sample auxiliaries are required.

Likewise for imaging **the scattering from the sample propagating** at an angle to the optical axis of the incoming beam (in classical optics known as dark field imaging) this approach of positioning the detector in close proximity of the sample does not work. For small angle scattering contrast (Strobl *et al.*, 2017) as well as diffraction based imaging (Woracek *et al.*, 2018), distance is required to obtain the required angu-

lar resolution. Spatial discrimination is then obtained by inserting slits or collimators or phase grids into the beam path, and mapping is provided by scanning the sample.

The classical optical approach to imaging at a distance is to use lenses. A range of optical devices have been demonstrated for focusing neutron beams based on **neutron guides**, capillary optics (Chen *et al.*, 1992), Fresnel zone plates (Altissimo *et al.*, 2004), compound refractive lenses (CRLs Eskildsen *et al.*, 1998) Wolter optics (Mildner & Gubarev, 2011) and sextupole magnets (Suzuki *et al.*, 2004). Evidently spatial mapping can be made with such focused beams by placing the sample in the focal plane and scanning it with respect to the beam. However, this is a tedious approach, and for time resolved work, the fact that different sub-volumes of the sample are probed at different times can be troublesome. Another solution is to place the sample downstream of the focal spot and generate a magnified image by projection microscopy. In both cases the spatial resolution is ultimately limited by the focal spot size.

Neutron full field microscopy is an alternative. Here the entire volume of interest in the sample is illuminated and an objective lens is introduced between the sample and the detector. As always for classical microscopy an inverted and potentially magnified or demagnified image forms in the image plane. Using CRLs proof-of-concept studies have been presented (Beguiristain *et al.*, 2002) and it has been demonstrated that the objective lens can discriminate against scattered neutrons to enable absorption contrast imaging from hydrogenous objects (Cremer *et al.*, 2005). To our knowledge, however, full field neutron microscopy has been applied only infrequently, if at all, presumably because only a fraction of the neutrons in the incoming beam is used, leading to signal-to-noise ( $S/N$ ) issues. In contrast, CRLs have seen extensive use at synchrotron sources (Snigirev *et al.*, 1996) as condensers, objectives and for

hard x-ray microscopes (Simons *et al.*, 2015).

In this paper we revisit the concept of a neutron microscope with CRL type objectives. In contrast to the synchrotron case, we show that such a neutron CRL often can be described as a lens with no attenuation, and with a resulting field-of-view (*FOV*) which is much larger than the physical aperture. With this insight we discuss optimisation of lens design. Next, we propose imaging configurations that optimize the throughput, i.e. the fraction of neutrons in the primary beam that contribute to the final image. We introduce the concepts of a kinoform lens and of a CRL array: an optics system comprising a 2D grid of CRLs with either parallel or diverging optical axes. Likewise we discuss solutions to overcome the issue of chromatic aberration. The focus is primarily on the design of the objective, as an optimisation of the incoming beam may involve other types of optics, such as supermirror based focusing.

Initially we present optical properties for candidate materials for CRL production and briefly discuss feasibility of manufacturing. Next, we introduce analytical expressions for the relevant optical parameters and define a figure-of-merit, *FOM*, for the overall efficiency of the imaging system. Following the presentation of several new optics concepts aimed at improving *FOM*, we illustrate the potential use of CRL based neutron microscopy by discussing solutions for bright field microscopy, depth resolved imaging, Small Angle Neutron Scattering (SANS) microscopy, grain mapping, and mapping of local strain from powder diffraction signals. Finally, we demonstrate some of the basic properties of neutron full field imaging for a single CRL in an experiment performed at the BOA test instrument at PSI.

## 2. Optical properties of a neutron CRL and imaging system

### 2.1. Candidate materials

Candidate materials for neutron CRLs have a large ratio  $\delta/\mu$ , where  $\delta$  is the refractive index increment and  $\mu$  is the linear attenuation coefficient, as calculated from the incoherent and absorption cross sections,  $\sigma_{\text{inc}}$  and  $\sigma_{\text{abs}}$ , respectively (Eskildsen *et al.*, 1998). Moreover the materials should be crystalline to avoid an otherwise massive attenuation due to the coherent cross sections  $\sigma_{\text{coh}}$  (all practical CRL materials have  $\sigma_{\text{coh}} \gg \sigma_{\text{inc}} + \sigma_{\text{abs}}$ ). A selection of candidate materials is presented in Table 1. Moreover, oxides and fluorides of Be, Bi, Pb are interesting. Be is in the following treated as a reference material, as Be has superior properties for neutron CRLs and at the same time lenses with very high accuracy are commercially available — as they are the preferred material for synchrotron use. However, Be is difficult to manufacture and existing lenses are costly.

Among the other materials crystals of  $\text{MgF}_2$  (Eskildsen *et al.*, 1998) and  $\text{SiO}_2$  (Gähler *et al.*, 1980) are easily available and can be machined by traditional milling machines. We argue that the resulting accuracy of approximately  $5 \mu\text{m}$  in general will be sufficient, for spatial resolutions in the 20–1000  $\mu\text{m}$  range. Moreover, we speculate that CRLs of  $^{208}\text{Pb}$  (or natural

Pb) and Bi can be cast, that CRLs in graphite can be made by powder compacting, and lenses in diamond made by laser ablation. In all cases, spurious effects such as small angle scattering would have to be characterised, and process optimisation may be necessary.

With so many materials and technologies at hand we argue that batch production of neutron CRLs with complicated 3D shapes should be possible, and discuss methodologies that require such configurations.

**Table 1**

Comparison of CRL candidate materials.  $\rho$  is density.  $\delta$  is the refractive index increment.  $\sigma_{\text{inc}}$  and  $\sigma_{\text{abs}}$  are the incoherent and the absorption cross sections, respectively — listed in (Sears, 1992) — and  $\mu$  is the linear attenuation coefficient. The numbers for C represents diamond. The first row refers to x-rays with 17 keV energy, while data for the neutron set-ups in the rows below relate to a wavelength of 4 Å.

	$\rho$ g/cm <sup>3</sup>	$\delta$ 10 <sup>-6</sup>	$\sigma_{\text{inc}}$ barn	$\sigma_{\text{abs}}$ barn	$\mu$ m <sup>-1</sup>
X-ray Be	1.85	1.25			46
Be	1.85	24.4	0.0018	0.0076	0.12
C	3.51	29.3	0.001	0.0035	0.08
MgF <sub>2</sub>	3.15	12.6	0.08	0.065	0.44
Bi	9.78	5.95	0.0084	0.038	0.13
<sup>208</sup> Pb	11.3	7.79	0	0.00048	< 0.01
SiO <sub>2</sub>	2.65	10.6	0.004	0.171	0.28

It is instructive to compare to the x-ray case. Comparing the tabulated numbers in the first line of Table 1 with the rest it is apparent that the ratio  $\delta/\mu$  is more favourable for neutrons, and that the attenuation is at least 2 orders of magnitude smaller for neutrons. This implies that a neutron CRL for the same focal length and physical aperture is much closer to the classical thin lens behaviour, i.e. the transmission of the lens will be limited by the physical aperture rather than attenuation in the lens material.

## 2.2. Geometry of a single neutron CRL

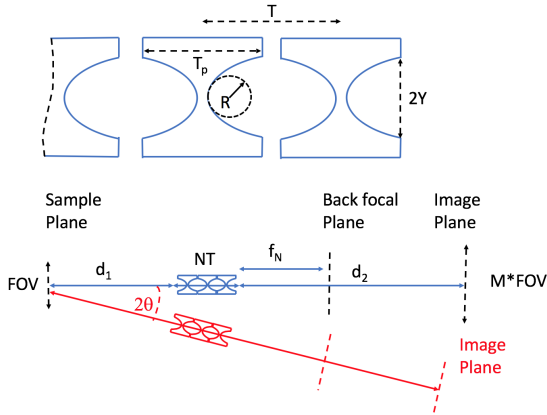


**Figure 1**

Above: geometry of a neutron compound refractive lens with  $N$  lenslets. The distance between lenslets,  $T$ , the physical thickness of each lenslet,  $T_p$ , the radius of curvature at the apex,  $R$ , and the physical aperture,  $2Y$ , are marked. Below: Geometry of bright field (blue) and diffraction based (red) neutron microscopy.  $2\theta$  is the scattering angle,  $d_1$  is the distance from sample plane to entry point of the objective,  $d_2$  the distance from the exit point of the objective to the image plane and  $f_N$  the focal length of the objective.  $M$  and  $FOV$  symbolises the magnification and field-of-view, respectively.

A comprehensive treatment of x-ray and neutron CRLs is presented in Cremer (2012). Here we will apply a formalism that has been developed for the hard x-ray microscope at ESRF, as this introduces equations for chromatic aberration.

The geometry is illustrated in Fig.1. We shall consider a two-dimensional CRL with  $N$  identical parabolic shaped lenslets, with a distance  $T$  between centers, each with radius-of-curvature of  $R$  and a physical thickness  $T_p \leq T$ . The focal length of each lenslet is then  $f = R/(2\delta)$ . The physical aperture is given by the diameter  $2Y = 2\sqrt{RT_p}$ , and we shall assume neutrons at distances to the optical axes that are larger than  $2Y$  to be absorbed by circular slits placed at the entry and exit of the CRL. The focal length of the entire CRL is  $f_N$  and the numerical aperture is  $NA$  (as defined by the FWHM).

The geometry of the imaging set-up is also illustrated in Fig.1. The magnification  $\mathcal{M}$  and the field-of-view  $FOV$  in the sample (as defined by the FWHM) are determined by the distances  $d_1$  and  $d_2$ .

The relevant optical parameters can all be determined by geometrical optics, and more specifically by the use of ray tracing by means of e.g. the ray matrix transfer formalism (Cremer, 2012; Poulsen *et al.*, 2014; Simons *et al.*, 2017) or by Monte Carlo methods (Willendrup *et al.*, 2014). For reference use we provide analytical expressions for the optical parameters for some general and special cases. In the *thin lens case*, with  $NT \ll f_N$  we have

$$f_N = f/N; \quad \mathcal{M} = \frac{d_2}{d_1}; \quad (1)$$

The same equations for the general *thick lens case* are derived

in (Simons *et al.*, 2017):

$$f_N = f\varphi \cot(N\varphi) \quad (2)$$

$$\mathcal{M} = \frac{1}{\cos(N\varphi)} \frac{f_N}{d_1 - f_N} = \cos(N\varphi) \frac{d_2 - f_N}{f_N} \quad (3)$$

Here  $\varphi = \sqrt{T/f}$ . For  $T = T_p$  this leads to  $f\varphi = Y/\sqrt{2\delta}$ .

Next we define the *transparent lens case* as the (thin or thick lens) case where the attenuation of the neutrons within the parabolic part is negligible. Key optical properties are then given by the dimensions of the entire CRL: that is by the physical aperture  $2Y$  and by the length of the CRL  $NT$ . We have  $N\varphi = \sqrt{2\delta} \frac{N T_p}{T}$ , where the last factor typically is close to 1. Moreover,

$$NA = \min \left( \frac{2Y}{d_1} \cos(N\varphi), 2\sqrt{2\delta} \sin(N\varphi) \right) \quad (4)$$

The first term reflects the limitation by the CRL as a collimator, the second term its limitation in terms of refractive power. The cosine factor in the first term originates in the fact that the neutron trajectory within the CRL approximately is a sinusoidal with period  $2\pi N\varphi$  (Poulsen *et al.*, 2017). Next we have

$$FOV = 2Y \cos(N\varphi) \left( \frac{d_1}{NT} + 1 \right) \quad (5)$$

We also define the *opaque lens case*, as the (thin or thick lens) case where the attenuation is so strong that the numerical aperture,  $NA$ , and the field-of-view,  $FOV$ , are determined by the parabolic section of the lens, and  $2Y$  is therefore so to speak irrelevant. The relevant equations are provided in Poulsen *et al.* (2017):

$$NA = 2.35\delta \frac{\mathcal{M}}{\mathcal{M} + 1} \left( \frac{2N}{\mu R} \right)^{1/2} \quad (6)$$

$$FOV = 2.35^2 \frac{2\delta}{\mu} \frac{1}{NA} \left[ (N\varphi)^2 - \sin^2(N\varphi) \right]^{-1/2} \quad (7)$$

The depth of field,  $DOF$ , is for neutrons defined exclusively by geometrical optics. In terms of the FWHM we have (for all lens cases)

$$DOF = \frac{y_s}{NA}. \quad (8)$$

Here  $y_s = y_d/\mathcal{M}$  is the spatial resolution in the sample plane, while  $y_d$  is the resolution in the imaging plane.

**Table 2**

Comparison of key optical properties for a CRL objective with lenslets of radius  $R = 50 \mu\text{m}$  and thickness  $T = 2 \text{ mm}$  for a focal length of  $f_N = 25 \text{ cm}$  and a magnification of  $\mathcal{M} = 10$ . The first row refers to x-rays with 17 keV energy, while data for the neutron set-ups in the rows below relate to a wavelength of  $4 \text{ \AA}$ .  $N$  is the number of lenslets. The three numbers listed for the Numerical Aperture,  $NA$ , and the Field-of-View,  $FOV$ , correspond to the FWHM for the transparent lens formalism, Eqs. 4 and 5, followed by the FWHM calculated by the opaque lens formalism, Eqs. 6 and 7, followed by results of McStas simulations.

	$N$	$NT$ mm	$NA$ (mrad) Trans/Opaq/McStas	$FOV$ (mm) Trans/Opaq/McStas
X-ray Be	71	142	2.5/ <b>0.68</b> /–	<b>1.3</b> / 1.7 /–
Be	4	8	<b>2.5</b> / 16 /2.97	<b>21</b> /1900/19.5
C	3	6	<b>2.5</b> / 18 /3.02	<b>25</b> /3100/22.7
MgF <sub>2</sub>	8	16	<b>2.5</b> / 12 /2.92	<b>11</b> / 380 /9.9
Bi	17	34	<b>2.5</b> / 8 /2.79	<b>5</b> / 720 /4.7
<sup>208</sup> Pb	13	26	<b>2.5</b> / 9 /2.75	<b>7</b> /1225/6.1
SiO <sub>2</sub>	9	18	<b>2.5</b> / 11 /2.89	<b>10</b> / /7.88

In Table 2, x-ray and neutron numbers for  $NT$ ,  $NA$  and  $FOV$  are compared for a specific setting, that has been frequently used for hard x-ray microscopy at beamline ID06 at ESRF (Simons *et al.*, 2015; Simons *et al.*, 2018). It appears that the  $NA$  for the neutron cases are 3.5 times larger than for the x-ray case, while the  $FOV$  is 5–20 times larger. Moreover the attenuation, which at most is  $\exp(-\mu NT/3)$ , is very small in the neutron case. (The tabulated values are for cold neutrons, as these are relevant for most of the applications presented. We have  $\delta/\mu \propto \lambda$ , where  $\lambda$  is the neutron wavelength.)

Finally, the transparent lens case is seen to be a good approximation for neutron work for the chosen geometrical setting. For all materials the  $NA$  is underestimated by 10%-20% in comparison to the McStas simulations, and the  $FOV$  correspondingly overestimated by a similar amount.

### 2.3. Chromatic aberration

Given the relatively large  $NA$ s of neutron CRLs, the intrinsic optical limit to the spatial resolution given by the diffraction theorem is below 100 nm, and as such truly negligible. In the following we shall assume that aberrations due to manufacturing errors of the lenses also are small. (For neutrons the spatial resolution is in fact often so relatively poor that the lenses can be manufactured with a spherical profile; the associated spherical aberration is negligible (Cremer, 2012).) The spatial resolution will then be given by the chromatic aberration, the detector pixel size and by the  $S/N$ . Let the FWHM of the blurring function associated with chromatic aberration be defined by a radius  $r$ , as measured in the sample plane. In the *thin lens limit* we have

$$r = \frac{\mathcal{M} + 1}{\mathcal{M}} Y \epsilon \quad (9)$$

where  $\epsilon = |\Delta E/E|$  is the relative energy bandwidth (FWHM).

In the true thick lens limit where the physical aperture does not play a role, the relevant equation for the root-mean-square

of the spread, RMS, in the sample plane is (Poulsen *et al.*, 2017)

$$\sigma_{\text{chr}} = \sigma_a \epsilon_{\text{RMS}} d_{\text{ch}} / \mathcal{M} \quad (10)$$

$$d_{\text{ch}} = N\varphi \left( \frac{d_1 d_2}{f\varphi} - f\varphi \right) \cos(N\varphi) \quad (11)$$

$$+ \left[ \frac{d_1 d_2}{f\varphi} + f\varphi + N\varphi(d_1 + d_2) \right] \sin(N\varphi),$$

where  $\sigma_a = NA/2.35$  is the RMS value for the numerical aperture, cf. Eq. 6, and  $\epsilon_{\text{RMS}} = \epsilon/2.35$ .

The chromatic aberration is clearly a critical issue for high spatial resolution bright field imaging work, but less so for low resolution work of relevance e.g. in diffraction based microscopy. As an example for a physical aperture of  $2Y = 5 \text{ mm}$  and a magnification of  $\mathcal{M} = 1$  the energy bandwidth can be 0.4%, 4% and 40% for a spatial resolution (FWHM) of  $10 \mu\text{m}$ ,  $100 \mu\text{m}$  and  $1 \text{ mm}$ , respectively.

For bright field microscopy it is actually possible to correct the lateral chromatic aberrations by focusing a condenser on the entry plane of the objective if the incident divergence is smaller than the  $NA$ . A very successful demonstration of this principle for hard x-rays was performed by Falch *et al.* (2016).

Using geometrical optics, the sample is assumed to be weakly scattering such that only absorption contrast is detected — in this context wide angle scattering, as e.g. in extinction contrast, is indistinguishable from absorption contrast, as the scattered radiation does not enter the objective lens. Within this framework it is possible find a relation between the position where a ray intersects the sample and its direction that minimizes the chromatic aberration in the detector plane. It turns out that the best solution is to focus the incident beam onto the entry plane of the CRL (Falch *et al.*, 2016). An improvement in resolution can only be achieved, however, when the random divergence of the incident beam is smaller than the  $NA$  of the CRL.

A general solution will require the construction of a neutron achromat. In Poulsen *et al.* (2014) it is proposed to create such a component by combining a converging Fresnel zone plate and a diverging CRL. Using ray tracing it is shown that a wavelength dispersion of much less than 1% can be achieved over a 10% band gap (Poulsen *et al.*, 2014). This solution however is associated with several challenges. Firstly, to the knowledge of the authors it is difficult to match the two types of optics in terms of  $Y$ ,  $NA$ , and  $FOV$ . Moreover the transmission of the achromat will not be close to 1, as is the case for the CRL on its own. Finally, generalising the achromat solution to a 2D array is challenging. We shall not consider this achromat solution in the rest of this manuscript.

### 2.4. Back focal plane

As for any lens, a neutron CRL is associated with a Fourier plane placed at a distance of  $f_N$  from the exit of the CRL. There is a linear relation between coordinates  $(y_B, z_B)$  in this plane and angles  $(\xi_y, \xi_z)$  in the sample plane (Poulsen *et al.*, 2018):

$$y_B = \frac{f_N}{\cos(N\varphi)} \xi_y; \quad z_B = \frac{f_N}{\cos(N\varphi)} \xi_z. \quad (12)$$

Here  $\xi_y$  is the projection of the angle between a ray and the optical axis onto the  $y$ -axis and  $\xi_z$  is the projection onto the  $z$ -axis.

With focal lengths of order 1 m, an angular offset of 1 mrad corresponds to 1 mm in the back focal plane. Hence, the Fourier space resolution obtainable can be excellent.

## 2.5. Figure of merit for efficiency

Different science cases call for different compromises between spatial, angular and time resolution. In this paper the focus is on providing extensive 2D maps of a given spatial and angular resolution as fast as possible. The generalisation to 3D is foreseen to be via tomographic reconstruction methods. For bright field imaging an alternative is depth resolved methods, see 4.2, for diffraction based imaging (at scattering angles not too close to 0 or  $\pi$ ) an alternative is layer-by-layer reconstruction.

For a given spatial resolution in the sample,  $s$ , we introduce the figure-of-merit

$$FOM = \left(\frac{FOV}{s}\right)^2 * NA^2 * \epsilon(r < s) * \Theta_{CRL} * \Theta_{Det}(\mathcal{M}) \quad (13)$$

The first term defines the number of positions in the sample plane imaged simultaneously, the second the angular range covered and the third the maximum energy band width and therefore maximum chromatic aberration error that is acceptable given the spatial resolution.  $\Theta_{CRL}$  is the average transmission of the CRL and  $\Theta_{Det}$  is the quantum efficiency of the detector. We require the pixel size of the detector to be substantially smaller than  $\mathcal{M}s$ .

For a bright field experiment, ideally the field of view match the sample area of interest,  $NA$  match the divergence of the incoming beam, and  $\epsilon$  match the energy bandwidth provided while  $\Theta_{CRL} = \Theta_{Det} = 1$ .

## 2.6. Design of a single neutron CRL

In the transparent lens limit it follows from Eq. 4 and Eq. 3 that

$$2Y = NA d_1 \frac{1}{\cos(N\varphi)} = NA f_N \frac{1 + \mathcal{M} \cos(N\varphi)}{\mathcal{M} \cos(N\varphi)^2}; \quad (14)$$

As stated the maximum  $NA$  for a CRL is  $2\sqrt{2\delta}$  and requires large magnifications. Hence, given constraints on lab space ( $f_N < 1$  m) it is generally speaking impractical to make a neutron CRL with a physical aperture  $2Y$  larger than about 8 mm.

Next, reducing empty space between lenslets is favorable for all properties, and we shall in the rest of this section assume  $T = T_p$ . Then for the  $FOV$  in the combined transparent and thin lens limit we have

$$FOV = 4\delta \frac{f_N^2}{Y} \left(\frac{\mathcal{M} + 1}{\mathcal{M}}\right). \quad (15)$$

Hence, with increasing physical aperture, the  $FOV$  decreases. Moreover, the total thickness increases, and the chromatic aberration radius also increases (Eq. 9). In terms of the  $FOM$  as defined in Eq. 13 it appears that the small aperture configuration is preferable. As a result we have  $FOV \gg 2Y$ , cf. also Table 2.

The imaging set-up is then essentially a camera obscura set-up with a lens inserted at the pinhole. The insertion of a lens improves the spatial resolution.

From the equations it also follows that for specified  $f_N$  and  $\mathcal{M}$  the optical parameters and  $FOM$  does not depend directly on  $R$  and  $T_p$  but only on the product  $\sqrt{RT_p}$ . In terms of design, the optimal choice of  $R$  and  $T = T_p$  is therefore defined by manufacturing issues. This is also the case in the thick lens limit (Poulsen *et al.*, 2017).

## 3. Improving the efficiency

### 3.1. Kinoform lenses

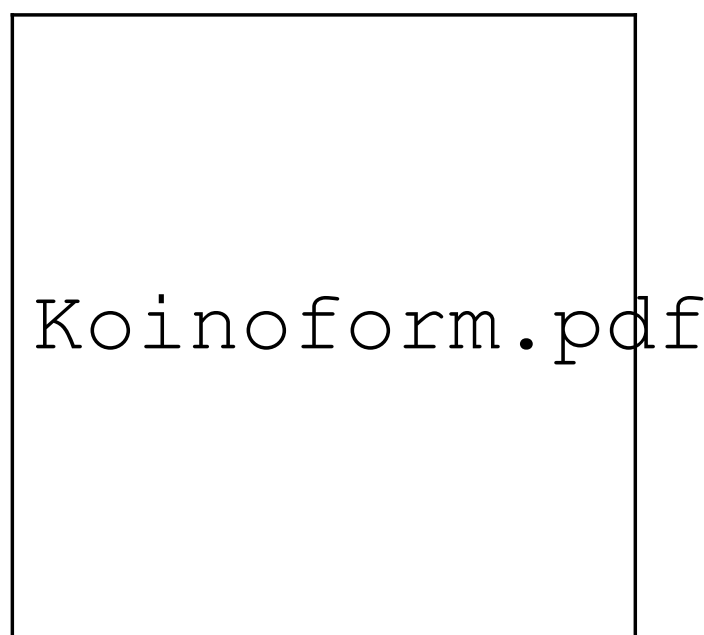


**Figure 2**  
Sketch of a kinoform lens. The first ten zones are marked.

A well known solution to increasing the physical aperture of a lens for a given focal length is to use a “kinoform” profile (Jordan *et al.*, 1970). Whereas the profile of each lens element in a CRL (see Fig. 1) was assumed to be parabolic in order to provide a phase shift  $\Delta\phi(r) = \frac{2\pi\delta}{R} r^2$ , in a kinoform lens the phase shift is taken modulo  $m2\pi$  ( $m \in \mathbb{N}$ ), resulting in a stepped profile with step height  $\Delta z_m = m\frac{\lambda}{\delta}$  as shown in Fig. 2.

The kinoform lens will provide an increased  $NA$  for a reduced thickness, at the expense of an increased issue with chromatic aberration, cf. Eq. 9. However, the introduction of steps in the lens profile also has disadvantages. The phase difference across the step can be made exactly  $m2\pi$  at only one wave length, due to the direct dependence of  $z_m$  on  $\lambda$  and the dispersion of the lens material,  $\delta(\lambda)$ . The error is cumulative, such that the zones will become progressively out of phase with the zeroth-zone beam. Furthermore, manufacturing limitations will introduce errors at each step. As the zones become more and more narrow away from the centre, the useful part (sufficiently far away from the inside and outside step) of the zone shrinks and

eventually vanishes. As the steps and their associated manufacturing errors may introduce artefacts and distortions in a direct image, we speculate that the main use of kinoform lenses will be as condensers and beam shaping elements.

### 3.2. Design of a 2D array of CRLs

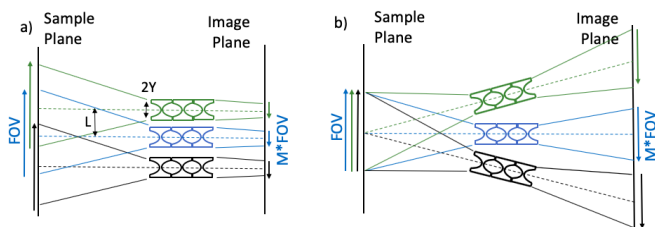


**Figure 3**

a) CRL array with parallel optical axes. b) CRL array with all optical axes coinciding in the sample plane.  $FOV$  is the field-of-view and  $M$  is the magnification.

An obvious way to increase  $FOM$  is to apply a number of CRLs in parallel, positioned in a 2D grid of say  $M \times M$  grid points. We shall call the resulting optical device a CRL array. It is of interest to use the same detector for several grid points, for reasons of cost and size of detector frame. Likewise it is of interest to manufacture the CRL array as one entity, which is pre-aligned, rather than  $M \times M$  independent CRLs, to be aligned individually. As discussed in section 2.1 there are several potential solutions to manufacture such complex optics.

Two examples of the configuration of a CRL array are illustrated in Fig. 3.

- *Parallel optical axes* of the CRL's. Let the distance between the centres of the holes be  $L$ , cf. Fig. 3, left. If we place the CRLs as close as possible we have  $L \approx 2Y$ . For  $M \geq 1$  and  $FOV \gg 2Y$ , it appears that a superposition of sub-images will take place in the image plane. These sub-images would have to be either disentangled or modelled as part of a forward projection algorithm.<sup>1</sup> For sparse images, typically related to diffraction based (dark field) microscopy, this may be feasible. However, for classical attenuation or phase contrast imaging the added complexity is hardly merited. For  $L \approx 2Y, \mathcal{M} < \frac{2Y}{FOV}$  there will be no superposition. Hence by demagnifying the image one may *sample both spatial and angular degrees of freedom almost fully*. However, this comes at the expense of smaller detector pixels (and therefore potentially associated with an inferior detector quantum efficiency) and a larger total number of pixels. Moreover for a high degree of demagnification ( $\mathcal{M} \ll 1$ ) the chromatic aberration deteriorates the resolution, cf. Eq. 9.
- *Divergent optical axes*. The manufacturing principles outlined above would allow for the various individual CRLs to have different optical axes. For some applica-

tions it may be favourable for the optical axes of the various CRLs to coincide in the Origo of the sample plane, cf. Fig. 3, right. In that way one can approach a  $4\pi$  coverage of the scattering from a given volume. The condition for a complete spatial and angular sampling is now for  $L \approx 2Y$

$$\frac{\mathcal{M}}{1 + \mathcal{M}} < \frac{2Y}{FOV}. \quad (16)$$

Still this comes at the cost of an increased number of pixels. In practice, the compromise between a large  $FOV$ , a large  $NA$  and small chromatic aberrations may lead to designs where the grid spacing  $L$  is substantially larger than  $2Y$ . Then the areas on the CRL array not participating in the focusing should be masked. Generally speaking the CRL array concept complies well with introduction of such masks.

## 4. Applications

In the following we aim to illustrate potential applications by comparing the  $FOM$  of CRL based full field microscopy solutions with the  $FOM$  of state-of-the-art instruments. Throughout we shall consider CRLs based on Be and neglect the efficiency of detectors, as we for sake of simplicity assume these to be the same.

### 4.1. Bright field imaging

One obvious application is for imaging in cases involving *bulky sample environments*. As an example consider imaging with polarised neutrons, where the polarisation analyser equipment requires an extended distance of say half a meter between sample and detector. As typical parameters for such measurements today (Strobl *et al.*, 2019) we shall consider imaging of a sample of dimension 2 cm. Using an energy bandwidth of 3% (given by the spin precession resolution), a spatial resolution of  $500 \mu\text{m}$  is achievable, corresponding to a divergence of the incoming beam of 1 mrad. Correspondingly  $FOM = (0.02 \text{ m}/0.0005 \text{ m})^2 \cdot 1 \text{ mrad}^2 \cdot 0.03 = 4.8 \cdot 10^{-5} \text{ rad}^2$ .

A microscope set-up with a sample-detector distance of 3 m and a 1:1 magnification leaves ample of space to put the polariser either between the sample and objective or between the objective and the detector. Using the thin lens formalism, Eqs. 4 and 9, a single CRL with  $N = 60$  Be lenslets with  $R = 2 \text{ mm}$  and  $T = 8 \text{ mm}$  would have  $f_N = 0.52 \text{ m}$ ,  $d_1 = 1.04 \text{ m}$ ,  $2Y = 8 \text{ mm}$ ,  $FOV = 2.5 \text{ cm}$ ,  $NT = 0.48 \text{ m}$ ,  $NA = 8 \text{ mrad}$  and  $\epsilon = 3\%$ . For this we have  $FOM = (0.02 \text{ m}/0.0005 \text{ m})^2 \cdot 8 \text{ mrad}^2 \cdot 0.03 = 0.0030 \text{ rad}^2$ . Hence, for the specified spatial resolution we have a gain of 65. Additional increase are possible using the achromat condenser and/or an array of identical CRLs configured in the fashion of Fig. 3 (right).

Another potential use is for *in-line phase contrast imaging* (Allman *et al.*, 2000) or alternatively for removing unwanted edge contrast effects in attenuation contrast images (Strobl *et al.*, 2008). Notably, the objective defines a specific plane perpendicular to the optical axis, the sample plane, cf. Fig. 1. Placing the exit edge of the sample at the sample plane will result in

<sup>1</sup> Within the CRL the path of a ray is sinusoidal. For small  $Y$  a non-inverted 1:1 image can be obtained. Then the sub-images can be merged. However, the  $NA$  would be small and the S/N therefore poor.

a pure attenuation image with no superposed fringes from phase contrast. Alternatively translating the sample along the optical axis pure in line phase contrast images can be obtained at any requested Fresnel number. Given the weak interaction of matter with thermal neutrons, the single image (one distance) algorithm by Paganin *et al.* (2002) for reconstructing both the phase and the amplitude can be expected to work. This was recently corroborated by applications in neutron tomography by Paganin *et al.* (2019).

#### 4.2. Depth resolved microscopy

In bio-imaging confocal microscopy is a powerful tool for mapping specimens in 3D without the use of sample rotations and tomographic reconstruction algorithms (Tiziani & Uhde, 1994). The large NA of classical light microscopy does in itself provide a depth resolution, but the emitted light from the layers out of focus deteriorates the image. In confocal microscopy the spurious light from these layers out of focus is much reduced. The drawback is that the method in its original form only provides information about one local volume at a time, and as such requires scanning of the beam or the sample in  $(x, y, z)$ . Current implementations relax this constraint by using a layer beam or multiplexing the output in other ways.

The relatively large NA of a neutron CRL objective and the weak interaction of thermal neutrons with many materials open up for a similar approach for neutron bright field imaging. For many specimens, in particular biological materials, the coherent cross section is much larger than the cross section for absorption. As such the use of an objective is a way to use the scattering signal to map the structure of the specimen, where the scattering acts as an internal source in the same way the fluorescent signal from the died molecules do in visual light microscopy. We speculate that neutrons from layers out of focus again will lead to a deterioration of the image. Transferring the principles of confocal microscopy to neutrons would then be a solution to improve image quality at the expense of data acquisition time.

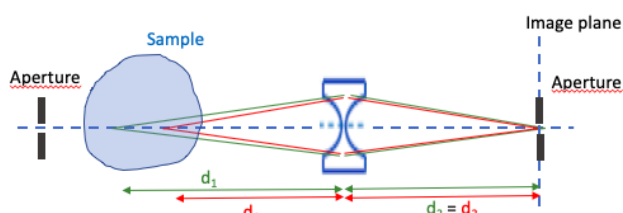


**Figure 4**

Basic set-up for confocal neutron microscopy. The incoming beam is a pencil beam, defined by an aperture and/or a condenser. It defines a line through the sample. This in connection with the imaging geometry defines one internal point in the sample, and remove stray scattering from neighbouring parts of the sample. A detector is placed after the aperture. The imaging configuration for two energies (green and red) are shown.

A basic set-up for neutron confocal microscopy is shown in Fig. 4. The nominal neutron wavelength,  $\lambda_0$ , is associated with

a sample plane and an image plane, defined by distance  $d_1^0$  and  $d_2$ , respectively. The sample plane for a slightly different wavelength,  $\lambda$ , is at  $d_1$ . In the thin lens approximation we have

$$\frac{d_1 - d_1^0}{d_1^0} = \frac{\mathcal{M}}{\mathcal{M} + 1} \left( \frac{\lambda_0^2}{\lambda^2} - 1 \right) \quad (17)$$

$$\approx -2 \frac{\mathcal{M}}{\mathcal{M} + 1} \frac{\lambda - \lambda_0}{\lambda_0} \quad (18)$$

Hence, various depths in sample can be probed simultaneously if the setting allows energy determination with sufficient accuracy. As mentioned 3D mapping is then achieved by scanning the sample with respect to the beam in  $(x, y, z)$ .

As an example consider an implementation where the incoming beam has dimensions of  $50 \mu\text{m} \times 50 \mu\text{m}$ ,  $NA = 10 \text{ mrad}$ ,  $f_N = 0.25 \text{ m}$  and the magnification is  $\mathcal{M} = 1$ . Then the depth of field is  $5 \text{ mm}$ , cf. Eq. 8. This corresponds to a  $2 \%$  change in the working distance  $d_1$ . According to Eq. 18 one can therefore generate a profile along the line with a resolution of  $5 \text{ mm}$ , provided the energy discrimination of the setup is better than  $2 \cdot 10^{-2}$ , which is realistic for TOF operation. In a different embodiment one may use the condenser achromat described in section 2.3. In this way one only maps one point at the time, but the S/N is improved.

Point by point scanning is evidently tedious, and similar to the situation for visual light, a compromise is required between suppression of signal from points out of focus and data acquisition time. The use of a layered incoming beam could be a place to start. Moreover, multiplexing can be obtained by using an objective array as in Fig. 3a.

#### 4.3. SANS microscopy

With x-rays imaging of the small angle x-ray scattering (SAXS) signal is a mature field. Scanning a sample with respect to a micro-beam this is used for studies of anisotropic systems such as bone, tree and hair (Gourrier *et al.*, 2007). Hard x-ray microscopy is a powerful alternative, used e.g. for providing 3D images of colloidal systems (Byelov *et al.*, 2013). With neutrons, SANS imaging by means of rastering the sample is used regularly, e.g. to study flow (Penfold & Tucker, 2007; Dewhurst & Grillo, 2016). CRLs are also used in SANS set-ups as condensers with the detector in the back focal plane of the lens.

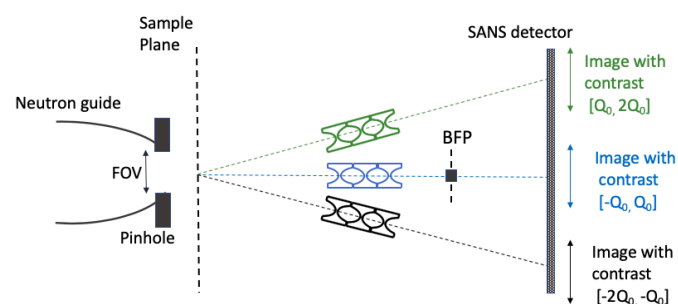


**Figure 5**

Proposed set-up for SANS microscopy. The CRLs all have a field-of-view (FOV) that matches the dimension of the incoming beam. The beam stop in the back focal plane (BFP) of the central CRL is used to remove the direct beam.

In Fig. 5 we sketch a SANS microscope. By adding CRLs this set-up will be able to cover the entire  $Q$ -range of interest. There are no moving parts and the CRL array can be added to an existing SANS instrument. The  $Q$ -resolution of each CRL (at fixed wavelength) is approximately  $\Delta Q = \frac{4\pi}{\lambda} \frac{NA}{2}$ . This is in the range of  $0.01 \text{ \AA}^{-1}$ , which matches the  $Q$ -resolution of SANS instruments (Dewhurst & Grillo, 2016). However, depending on the position within the sample plane there is an offset to the  $Q$ -range covered by a given CRL.

It appears that for  $FOV < 2Y/M$  (no overlap between the images from neighbouring CRLs, cf. section 3.2) essentially all the neutrons available for SANS is available also for SANS microscopy: one simply swaps between a set-up with no spatial resolution and high  $Q$ -resolution (classical SANS) and one with medium spatial resolution and medium to high  $Q$ -resolution (SANS microscopy). Moreover, for studying one specific region in  $Q$ , one may increase the  $FOV$  to become larger than  $2Y/M$ .

As an example of state-of-the-art we shall consider a rastering study of a mechanical pen performed at the D33 SANS instrument at ILL (Dewhurst & Grillo, 2016). For this a  $200 \mu\text{m}$  pinhole was inserted in front of the sample in a beam of 10% bandwidth and a divergence of 5 mrad. The SANS detector was positioned at 15 m from the sample. The contrast in  $Q$  was in this particular case defined by summing over the intensities in area detector, resulting in 3  $Q$ -intervals: low, medium and high  $Q$ 's. The low  $Q$ -range corresponded to an angle (FWHM) of 10 mrad. Hence, a figure-of-merit of this set-up is  $FOM = 1^2 \cdot (10 \text{ mrad})^2 \cdot 0.1 = 1.0 \cdot 10^{-5} \text{ rad}^2$ .

For the SANS microscope let us first consider the low  $Q$  range with the same incoming beam, but a pinhole of 30 mm. We shall assume that this only changes the divergence of the incoming beam by a negligible amount. We require a similar spatial resolution:  $200 \mu\text{m}$ . As an example of an implementation we consider a single Be CRL with  $Y = R = T_p = T = 0.0035 \text{ m}$ ,  $N = 91$  and 1:1 imaging. According to the transparent lens case this will be associated with  $f_N = 0.70 \text{ m}$ ,  $NT = 0.32 \text{ m}$ ,  $NA = 4.1 \text{ mrad}$ ,  $FOV = 30 \text{ mm}$ ,  $\epsilon = 2.8\%$ . The figure-of-merit of this set-up is  $FOM = (0.03/0.0002)^2 \cdot (4.1 \text{ mrad})^2 \cdot 0.028 = 0.0109 \text{ rad}^2$ . Hence, the gain is a factor of 1000. Note also that with the small incoming divergence a condenser achromat would be suitable.

For the higher  $Q$ -ranges, we have to use a CRL array and consequently we will reduce the  $FOV$  to  $2Y = 7 \text{ mm}$ , to avoid the overlap of images in the image plane. The gain is then of order 50.

Another potential application of SANS microscopy is the equivalent of tensor small angle x-ray scattering. Here, the anisotropy (or texture) of a small angle scattering pattern is measured during a 2D tomography scan — sample rotations about 2 orthogonal axes are needed in order to determine the full tensor anisotropy. In the x-ray case a micro-beam is rastered across the sample, and a full SAXS pattern is recorded at each point (Liebi *et al.*, 2015; Liebi *et al.*, 2018). We propose that equivalent data could be acquired by SANS microscopy using a lens array. A set of slits in the back-focal plane could be used to improve the angular resolution, e.g. to select a relevant length

scale. Each lens in the array then provides a real-space image corresponding to the range in azimuth collected by that particular lens. At least 4 lenses arranged in a ring are required for rank-2 tensor anisotropy, 8 lenses for rank 4, etc.

#### 4.4. Phase and strain mapping

Within materials science and geoscience it is of interest to map the crystalline phases in a sample in 3D and for a given phase to map the local texture and the strain tensor. The latter may be used for generation of a stress map. State-of-the-art instruments are monochromatic diffractometers such as STRESS-SPEC at FRM-II (Hofmann *et al.*, 2006; Hofmann *et al.*, 2013) and time-of-flight (TOF) diffractometers like VULCAN at SNS (Wang *et al.*, 2010), ENGIN-X at ISIS (Santisteban *et al.*, 2006) and the planned instrument BEER at ESS (Fenske *et al.*, 2016). Using slits and radial collimators these provide a large coverage of the scattering from one specified local volume. Mapping is then obtained by scanning the sample with respect to the beam in  $(x, y, z)$ .

The approach of a *neutron dark field microscope* is instead to map the relevant (sub)volume of the sample in one setting with no movements or rotations of the sample. This may speed up the entire data acquisition, thereby supporting time resolved measurements, or making industrial exploration cheaper.

In this section 4.4 we shall assume the diffracting elements within the sample to be sufficiently small that the scattered signal is that of a (textured) powder diffraction pattern. Moreover, we assume that the phases present either are known *a priori* or have been identified in other ways e.g. from neutron powder diffraction on the same sample.

A CRL array with the optical axes coinciding in the sample plane, cf. Fig. 3, right, can in principle be used to obtain a  $4\pi$  coverage of the scattering. Such a construction would comprise an inner shell of CRLs and an outer shell of detectors. This would be a very efficient collection of data.

Equally important, by providing projections from a number of directions, a 3D reconstruction can be obtained without any rotation of the sample. For this purpose a substantially reduced coverage is sufficient. The exact number of projections required and the optimal configuration will depend on the specifications for the microscope. To our knowledge such an optimisation has not been performed for a highly divergent white beam source.

In practice the merit of using a neutron dark field microscope depends on the ratio between the  $FOV$  and the dimension of the gauge volume,  $s$ . For coarse mapping of large components on a centimeter scale or for weak neutron sources it is not relevant. Another concern is that the CRL performance deteriorates with increasing neutron energy.

In the following we consider an implementation at a monochromatic source. If we place a CRL - with a circular aperture - in the diffraction beam at a scattering angle of  $2\theta$ , the resolution becomes  $\Delta 2\theta = \frac{\pi}{4} NA$  (FWHM). From this follows a strain resolution of

$$\left| \frac{\Delta d}{d} \right| = \frac{\pi}{8} \cot(\theta) NA \quad (19)$$

For  $NA = 5 \text{ mrad}$ , the resulting strain resolution at  $2\theta = \pi/2$

is  $2 \cdot 10^{-3}$ . To determine the average strain (within a voxel in the sample) with a higher accuracy than the resolution, one may interpolate or fit a model of the 'peak profile' to intensities associated with neighbouring  $2\theta$  bins, similar to how neutron strain scanning is performed today. Moreover the CRLs can be offset azimuthally. Notably, with an energy spread of say 3% and  $\mathcal{M} = 1$  the chromatic aberration is not an issue for  $s \geq 0.5$  mm and  $\mathcal{M} \leq 0.1$ , cf. Eq. 9.

Hence, it appears that conceptually one can think of a dark field microscope in terms of each of the individual radial collimators being replaced by a 1D stack of CRLs. To avoid overlap of images demagnification is required. The demagnification leads to long distances  $d_1$  and a large thickness  $NT$ .

The advantage is that angular and spatial degrees of freedom are separated and that one therefore can make a 2D map for each CRL. 2D mapping for a layer in the sample is then readily provided by using a line beam as incoming beam and 3D mapping by translating the sample with respect to the beam and stacking layers on top of each other. Moreover, the issue with pseudo peaks shifts due to partially filled gauge volumes, that has been discussed at length for neutron strain instruments (Pirling, 2011), is overcome in this way. The substantial disadvantages are the overhead of constructing a voluminous and heavy 'bank' of CRLs and the fact that the 2D detector must have a larger *FOV* and be equipped with more pixels. Also background will become more of an issue.

To illustrate the potential we compare with the state-of-the-art materials science diffractometer STRESS-SPEC at the FRM II reactor (Hofmann *et al.*, 2006; Hofmann *et al.*, 2013). Operating at  $2.3 \text{ \AA}$  with an energy spread of  $\epsilon = 3\%$ , the smallest gauge volume is  $(0.5 \text{ mm})^3$ . The corresponding radial collimator is placed at a distance of 15 cm, and therefore has a horizontal divergence of 3.3 mrad. It is 35 cm long and covers the full detector height vertically and 9 degrees in  $2\theta$  horizontally.

As an implementation of a dark field microscopy set-up at  $2.3 \text{ \AA}$  consider initially a vertical array of *one-dimensional* CRLs, in the configuration shown in Fig. 3b. We specify a demagnification of  $\mathcal{M} = 0.1$ , and space availability leads to  $d_1 = 2$  m. Let each CRL have  $N = 196$  lenslets and a relatively small physical aperture  $Y = T = T_p = R = 1$  mm. As a result  $NA = 5$  mrad and  $FOV = 14$  mm. With this setting the criterion of Eq. 14 is fulfilled, so overlap of sub-images is avoided. Moreover, let the horizontal width of these lenses be 6.6 mm. With such a setting, a 1D vertical array can replace one slot in the radial collimator, providing the same angular coverage and resolution. However, information is now provided in parallel for  $FOV/s = 28$  positions along the optical axis of the incoming beam instead of 1. In practice the gain will be lower, due to transmission losses and a lower S/N.

In a more advanced embodiment, the 1D lenses above are replaced with 2D lenses with the same specifications (a  $NA$  of 5 mrad in both directions) and the incoming beam is configured to be a line beam of dimensions  $14 \times 0.5 \text{ mm}^2$ . In this way an entire area of  $14 \times 14 \text{ mm}^2$  in one layer in the sample is mapped in one setting. At the same time the angular resolution in the  $2\theta$  direction is slightly improved to become 2.5 mrad.

#### 4.5. Mapping of grains and single crystals

For a monochromatic and parallel neutron beam, crystalline elements of a certain volume give rise to distinct diffraction spots at specified angular settings. Placed on a goniometer either the entire sample (in case of a single crystal) or an embedded grain can be reoriented such that the direction of the diffracted beam is aligned with the optical axis of the objective. The situation is then fully equivalent to the hard x-ray dark field microscopy set-up implemented at beamline ID06 at ESRF (Poulsen *et al.*, 2017; Simons *et al.*, 2015; Simons *et al.*, 2018). By scanning sample tilt angles maps of the local orientation can be mapped. In a polychromatic setting, the axial strain can be mapped by shifts in the energy spectrum, similar to the process outlined in section 4.4.

For a more complete coverage, to map say a grain with an internal degree of mosaicity larger than the  $NA$ , one may perform a continuous scan of a sample tilt stage while acquiring data and/or exploit the use of a CRL array. In this case, the data is sparse, and overlap of images is less of an issue.

The reciprocal space resolution of a dark field microscope for elastic scattering is described in detail in (Poulsen *et al.*, 2017). For neutrons the resolution function will tend to be an isotropic Gaussian, except for  $2\theta$  near 0 and  $\pi$ . For points off the optical axis the centre point for the reciprocal space resolution function shifts. Moreover, it should be noted that acquiring images while scanning one of the sample tilts will not ensure a uniform sampling of reciprocal space. Strategies for coping with these issues are discussed in (Poulsen *et al.*, 2017).

A prerequisite to using the dark field microscope for grain mapping is that the grain, and its orientation has been identified. Multigrain indexing methods similar to those developed for x-rays (Sørensen *et al.*, 2012) are therefore required. In Peetermans *et al.* (2014) and Cereser *et al.* (2017) such methodologies are described for neutrons, in a low resolution and TOF setting, respectively. Similar to the x-ray case there is a strong degree of complementarity between such tomographic methods providing an overview of the entire specimen and dark field microscopy, focusing on only one grain at a time.

#### 5. Experimental demonstration

A demonstration of bright field neutron microscopy using a CRL as objective was performed using an ad hoc set up at the BOA test instrument at PSI. Using a double-bounce pyrolytic graphite monochromator **with a mosaicity of 100 arcminutes** a beam was created with an average wavelength of  $4 \text{ \AA}$  and an energy bandwidth of 3%. From McStas simulations we estimate a divergence of the exit beam  $\alpha_v = 7.4$  mrad (vertical)  $\times \alpha_h = 20$  mrad (horizontal). The sample was a Gd reference pattern: a star with 36 spokes, see Fig 5 b). The illuminated area was limited by absorbers in the set-up, but provided a near uniform illumination.

The Be CRL was configured as follows:  $N = 4$ ,  $R = 50 \mu\text{m}$ ,  $T = 2$  mm,  $T_p = 1$  mm and hence  $2Y = 0.45$  mm. To avoid scattering through the non-convex parts of the CRL two Gd pinholes were placed at the entry and exit of the CRL. The same CRL has been used for x-ray microscopy with a resulting spatial resolution of about 100 nm. The 2D detector was a PSI midibox type

scintillator-camera detector with a 200 micrometer thick LiF/ZS scintillator coupled to an Andor iKON M camera. The pixel size was 0.105 mm. We determined the intrinsic point-spread-function to have a width of  $440\mu\text{m}$  (FWHM). The sample-CRL entry and CRL exit-detector distances were  $d_1 = 0.38$  m and  $d_2 = 0.76$  m, respectively, while the magnification was determined experimentally to be  $\mathcal{M} = 2.18$ .

In the transparent lens limit this leads to  $f_N = 256$  mm,  $NA = 1.2$  mrad and  $FOV = 21.8$  mm. Moreover  $NT/f_N = 0.03$ , so we are clearly in the thin lens limit. The corresponding estimate for the radius of the blurring function associated with chromatic aberration is  $r = 4.6\mu\text{m}$ .

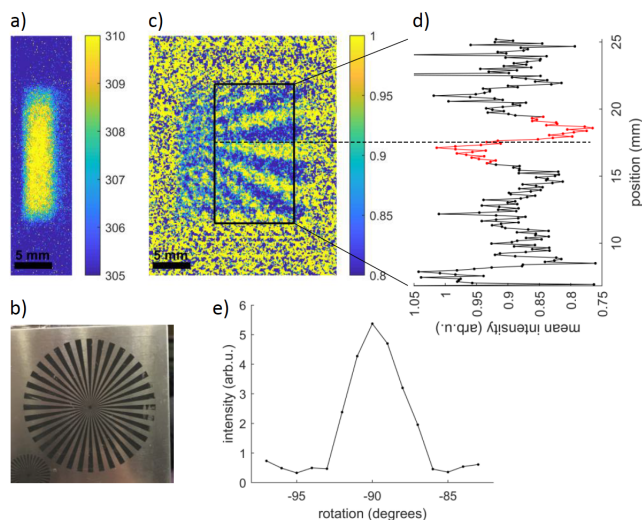


**Figure 6**

Bright field microscopy demonstration. a) A raw image without sample with colours representing intensity in arb. units, b) the Gd Siemens star type reference sample (a normalised image with colours indicating intensities in arb. units), c) an image of the sample stitched together from individual images acquired while scanning the sample, and d) a vertical intensity profile across spokes. In e) is shown the intensity of the entire image as function of rotation angle, when rotating around the vertical axis, perpendicular to the incoming beam.

An image acquired with the sample removed is shown in Fig 5 a). The resulting field-of-view in the sample plane is 7.7 mm x 2.0 mm (FWHM). Given the point-spread function of the detector there is no sign of vignetting in the optical system. Next the sample was inserted and scanned in the horizontal direction. A resulting stitched image is shown in Fig 5 c). As expected the image is non-distorted apart from an overall blurring, which appears to be Lorentzian and to be approximately uniform over the image. The FWHM is 0.67 mm. Subtracting the point-spread-function of the detector, and dividing by the magnification, we reach a rough estimate of the blurring due to the optical set-up. The result is a blurring function with a radius of 0.05 mm in the sample plane.

Next the sample was rotated around a vertical axis, perpendicular to the beam. The intensity integrated over the entire detector is shown as function of rotation angle in Fig 5 e). The width of the intensity profile is  $64 \pm 10$  mrad. In the

transparent lens limit this should be compared to a width of  $\sqrt{\alpha_h^2 + \frac{2Y}{NT}} = 55$  mrad.

In summary, the set-up could be optimized in several ways. In particular we speculate that the decrease in resolution is due to geometrical errors related to the entry and exit holes in the CRL. Nevertheless, the results demonstrate the pertinent features outlined above: the validity of applying the transparent lens limit and the fact that the  $FOV$  is much larger than the physical aperture and the resolution.

## 6. Discussion

In contrast to imaging with many other probes, imaging with neutrons today relies almost entirely on lensless techniques. Imaging in a pinhole geometry does provide a high flexibility with respect to the field of view and spatial resolution based on the spectrum and beam divergence available. However, neutron imaging has diversified significantly in recent years, methodically as well as with respect to applications. This diversity, together with successful applications in synchrotron x-ray imaging, has motivated this work where we explore the use of neutron full field imaging by means of inserting an objective between the sample and the detector. The anticipated low cost and high degree of adaptability has moved us to focus on CRLs, but much of the formalism established and some of the new modalities introduced are relevant also for objectives based on e.g. zone plates or Wolter optics. (For a recent full field microscopy demonstration experiment using Wolter optics, see Jorba *et al.* (2019)).

A main shortcoming of refractive optics is the limit on physical aperture and numerical aperture given by the refractive power. We show here that these in principle can be overcome by the introduction of CRL arrays. Another shortcoming is the chromatic aberration. Here we show that for medium-to-low spatial resolution work, the loss may be acceptable. The relevance of full field microscopy as described above is instead whether the science case demands and the available neutron flux supports a large ratio between field-of-view and spatial resolution. Here the cases of bright field at a distance, SANS, and diffraction from large crystals tend to have a flux advantage in comparison to the case of powder diffraction. Moreover, for bright field imaging, achromaticity can be ensured by focusing a condensed on the entry plane of the objective.

The gain in  $FOM$  with respect to existing instruments will depend strongly on science case, sample details and details of the current implementation. For these reasons the gains calculated in the examples above serve only as order-of-magnitude estimates. In particular, we point out that we have neglected several issues with S/N and background noise, as these are dependent on details of detectors and screening.

As a next step we propose to establish whether one or more of the manufacturing routes suggested can be developed to the stage where serial production is feasible, with specifications as presented here. In that connection, a better understanding of the requirement to crystallinity is required. Polycrystalline lenses with large grains will lead to glitches in the spectrum (Zhang *et al.*, 2019), while nanocrystalline grains will lead to massive

secondary extinction and consequently an orders of magnitude increase in the effective attenuation. The acceptable range needs to be determined. Another step forward would be full scale simulations of entire microscopes - with optimised condensers and objectives - using e.g. Monte Carlo methods.

One end goal is to enable CRL based condensers and objectives being used to retrofit existing instruments. In that context we mention that for small  $Y$  an entire imaging system can be relatively confined. A more ambitious aim is to prepare for a general purpose neutron microscope, with banks of objectives and detectors covering bright field, SANS and wide angle diffraction in one set-up.

## 7. Conclusion

The cross sections for thermal neutrons are different from those of visual light, x-rays and electrons, both in terms of magnitude and ratio between absorption, coherent and incoherent scattering. At the same time, neutron sources are essentially  $4\pi$  polychromatic sources, in contrast to the heavily collimated and monochromatic beams of lasers, undulator peaks at synchrotrons and electron microscopes. In this paper we have explored the virtue of transferring well established optical components and imaging systems for full field microscopy with refractive elements from these other fields to neutron imaging. We find that

- A geometrical optics description in terms of a "transparent lens" is in general adequate for a coarse design.
- The accuracy of simple manufacturing methods such as machining is believed to be sufficient for a spatial resolution of  $20\ \mu\text{m}$  and up. This in connection with the high ratio of  $\delta/\mu$  allows for complicated optical designs providing large coverage in direct space or angular space.
- For a single CRL and at  $4\ \text{\AA}$  the numerical aperture is limited by the refractive power to be around  $10\ \text{mrad}$ , while the physical aperture is below  $1\ \text{cm}$ . The  $FOV$  on the other hand can be much larger than the physical aperture. We suggest that  $NA$  and  $2Y$  can be improved by construction of kinoform lenses and/or CRL arrays.
- In comparison to existing neutron imaging instruments, the  $FOM$  is typically degraded in terms of angular acceptance and energy bandwidth when introducing a CRL objective. Nevertheless, we have illustrated that for a range of medium-to-low spatial resolution applications a resulting gain in  $FOM$  by several orders of magnitude is possible, due to the simultaneous mapping of the properties in many parts of the sample. The simultaneous registration is also seen as an asset in itself for time resolved studies.
- For diffraction based imaging, an objective based solution has the fundamental advantage that spatial and angular degrees of freedom decouple. Similar to work in a transmission electron microscope one may use slits in the back focal plane to define a specific volume in reciprocal space, and then provide imaging corresponding to this  $Q$ -space contrast.
- For bright field imaging, an objective based solution has the advantage that an image is provided of a specific

plane, the sample plane. This may be used to avoid or access phase contrast. Moreover, the numerical aperture is sufficiently large that depth resolved imaging seems realistic, with a resolution of a few millimetres.

- For bright field imaging, partial correction of the chromatic aberrations increases the maximum band width usable without degrading the image, thus improving the efficiency of the imaging setup.

We thank PSI for the beamtime at BOA, ESRF for providing the Be lenslets, Emmanouela Rantsiou for help with the set-up at PSI, Pavel Trtik for borrowing the Siemens star sample, Christian David and Nikolaj Zangenberg for scientific discussions and Peter Willendrup for help with the McStas simulations. HL acknowledges a grant from Innovation Foundation Denmark.

## References

- Allman, B., McMahon, P., Nugent, K. A., Paganin, D., Jacobson, D., Arif, M. & Werner, S. (2000). *Nature*, **408**, 158–159.
- Altissimo, M., Petrillo, C., Sacchetti, F., Ott, F. & Di Fabrizio, E. (2004). *Microelec. Eng.* **73–74**, 644–650.
- Beguiristain, H. R., Anderson, I. S. & Dewhurst, C. D. (2002). *Appl. Phys. Lett.* **81**, 4290.
- Byelov, D. V., Meijer, J.-M., Snigireva, I., Snigirev, A., Rossi, L., van den Pol, E., Kuijk, A., Philipse, A., Imhof, A., van Blaaderen, A., Vroegeer, G. J. & Petukhov, A. V. (2013). *RSC Advances*, **3**, 15670–15677.
- Cereser, A., Strobl, M., Hall, S. A., Steuwer, A., Kiyangi, R., Tremisin, A. S., Knudsen, E. B., Shinohara, T., Willendrup, P. K., da Silva Fanta, A. B., Iyengar, S., Larsen, P. M., Hanashima, T., Moyoshi, T., Kadletz, P. M., Krooß, P., Niendorf, T., Sales, M., Schmahl, W. W. & Schmidt, S. (2017). *Sci. Rep.* **7**, 9561.
- Chen, H., Downing, R. G., Mildner, D. F. R., Gibson, W. M., Kumakhov, M. A., Ponomarev, I. Y. & Gubarev, M. V. (1992). *Nature*, **357**, 391.
- Cremer, J. (2012). *Advances in Imaging and Electron Physics*, **172**, 335–427.
- Cremer, J. T., Piestrup, M. A., Park, H., Gary, C. K., Pantell, R. H., Glinka, C. J. & Barker, J. G. (2005). *Appl. Phys. Lett.* **87**, 161913.
- Dewhurst, C. D. & Grillo, I. (2016). *J. Appl. Cryst.* **49**, 736–742.
- Eskildsen, M. R., Gammel, P. L., Isaacs, E. D., Detlefs, C., Mortensen, K. & Bishop, D. J. (1998). *Nature*, **391**, 563.
- Falch, K., Detlefs, C., DiMichiel, M., Snigireva, I., Snigirev, A. & Mathiesen, R. (2016). *Appl. Phys. Lett.* **109**, 054103.
- Fenske, J., Rouijaa, M., Saroun, J., Kampmann, R., Staron, P., Nowak, G., Pilch, J., Beran, P., Sittner, P. and, Strunz, P., Brokmeier, H.-G., Ryukhtin, V., Kaderavek, L., Strobl, M., Muller, M., Lukas, P. & Schreyer, A. (2016). *J. Physics Conf.* **746**, 012009.
- Gähler, R., Kalus, J. & Mampe, W. (1980). *J. Phys. E*, **13**, 546.
- Gourrier, A., Wagermaier, W., Burghammer, M., Lammie, D., Gupta, H. S., Franzl, P., Riekel, C., Wess, T. J. & Paris, O. (2007). *J. Appl. Cryst.* **40**, s78–s82.
- Hofmann, A., Gan, W. M., Rebelo-Kornmeier, J. & Schöbel, M. (2013). *Neutron News*, **24**, 14–17.
- Hofmann, M., Schneider, R., Seidl, G., Rebelo-Kornmeier, J., Wimporoy, R., Garbe, R. & Brokmeier, H.-G. (2006). *Physica B*, **385–386**, 1035–1037.
- Jorba, P., Schulz, M., Hussey, D., Abir, M., Seifert, M., Tsurkan, V., Loidl, A., Plederer, C. & Khaykovich, B. (2019). *J. Magn. Magn. Mater.* **475**, 176–183.
- Jordan, Jr., J. A., Hirsch, P. M., Lesem, L. B. & Van Rooy, D. L. (1970). *Appl. Opt.* **9**, 1883.
- Kallmann, H. (1948). *Research*, **1**, 254–260.
- Kardjilov, N., Manke, I., Strobl, M., Hilger, A., Treimer, W., Meissner, M., Krist, T. & Banhart, J. (2008). *Nature Physics*, **4**, 399–403.
- Kardjilov, N., Manke, I., Woracek, R., Hilger, A. & Banhart, J. (2018). *Materials Today*, **21**, 652–672.
- Lehmann, E. (2015). *Neutron News*, **26**(2), 6–10.

- Lehmann, E. H., Peetermans, S., Josic, L., Leber, H. & van Swygenhoven, H. (2014). *Nucl. Instrum. Meth. A*, **735**, 102.
- Liebi, M., Georgiadis, M., Kohlbrecher, J., Holler, M., Raabe, J., Usov, I., Menzel, A., Schneider, P., Bunk, O. & Guizar-Sicairos, M. (2018). *Acta Cryst. A*, **74**(1), 12–24.
- Liebi, M., Georgiadis, M., Menzel, A., Schneider, P., Kohlbrecher, J., Bunk, O. & Guizar-Sicairos, M. (2015). *Nature*, **527**(7578), 349–352.
- Mildner, D. F. R. & Gubarev, M. V. (2011). *Nucl. Instrum. Methods A*, **634**, S7–S11.
- Paganin, D., Mayo, S., Gureyev, T., Miller, P. & Wilkins, S. (2002). *J. Microscopy*, **206**, 33–40.
- Paganin, D., Sales, M., Beltran, M., Poulsen, H. & Schmidt, S. (2019). *In preparation*.
- Peetermans, S., King, A., Ludwig, W., Reischig, P. & Lehmann, E. H. (2014). *Analyst*, **139**, 5767–5771.
- Penfold, J. & Tucker, I. (2007). *J. Phys. Chem. B*, **111**, 9496–9503.
- Pirling, T. (2011). *Proc. Engineering*, **10**, 2147–2152.
- Poulsen, H. F., Cook, P. K., Leemreize, H., Pedersen, A. F., Yildirim, C., Kutsal, M., Jakobsen, A. C., Trujillo, J. X., Ormstrup, J. & Detlefs, C. (2018). *J. Appl. Cryst.* **51**, 1428–1436.
- Poulsen, H. F., Jakobsen, A. C., Simons, H., Ahl, S. R., Cook, P. K. & Detlefs, C. (2017). *J. Appl. Cryst.* **50**, 1441.
- Poulsen, S. O., Poulsen, H. F. & Bentley, P. M. (2014). *Nucl. Instrum. Meth. Phys. Res. A*, **767**, 415–420.
- Sales, M., Shinohara, T., Sørensen, M. K., Knudsen, E. B., Tremsin, A., Strobl, M. & Schmidt, S. (2019). *Journal of physics D*, **52**, 205001.
- Santisteban, J. R., Daymond, M. R., James, J. A. & Edwards, L. (2006). *J. Appl. Cryst.* **39**, 812–825.
- Santisteban, J. R., Edwards, L., Steuwer, A. & Withers, P. J. (2001). *J. Appl. Cryst.* **34**, 289–297.
- Schulz, M., Neubauer, A., Masalovich, S., Mühlbauer, M., Calzada, E., Schillinger, B., Pfeiderer, C. & Böni, P. (2010). *J. Phys.: Conf. Series*, **211**, 012025.
- Sears, V. F. (1992). *Neutron News*, **3**(3), 26–37.
- Simons, H., Ahl, S. R., Poulsen, H. F. & Detlefs, C. (2017). *J. Synchrotron Rad.* **24**(2), 392.
- Simons, H., Haugen, A. B., Jakobsen, A. C., Schmidt, S., Stöhr, F., Majkut, M., Detlefs, C., Daniels, J. E., Damjanovic, D. & Poulsen, H. F. (2018). *Nat. Materials*, **17**, 814–819.
- Simons, H., King, A., Ludwig, W., Detlefs, C., Pantleon, W., Schmidt, S., Stöhr, F., Snigireva, I., Snigirev, A. & Poulsen, H. F. (2015). *Nat. Commun.* **6**, 6098.
- Snigirev, A., Kohn, V. G., Snigireva, I. I. & Lengeler, B. (1996). *Nature*, **384**, 49.
- Sørensen, H. O., Schmidt, S., Wright, J. P., Vaughan, G. B. M., Techert, S., Garman, E. F., Oddershede, J., Davaasambu, J., Paithankar, K. S., Gundlach, C. & Poulsen, H. F. (2012). *Z. Kristallogr.* **227**, 63–78.
- Strobl, M., Harti, R., Grünzweig, C., Woracek, R. & Plomp, J. (2017). *J. Imaging*, **3**, 64.
- Strobl, M., Heimonen, H., Schmidt, S., Sales, M., Kardjilov, N., Hilger, A., Manke, I., Shinohara, T. & Valsecchi, J. (2019). *Journal of Physics D: Applied Physics*, **52**(12), 123001.
- Strobl, M., Manke, I., Kardjilov, N., Hilger, A., Dawson, M. & Banhart, J. (2009). *J. Phys. D*, **42**, 243001.
- Strobl, M., Treimer, W., Kardjilov, N., Hilger, A. & Zabler, S. (2008). *Nucl. Instrum. Methods B*, **266**, 181.
- Suzuki, J.-i., Oku, T., Adachi, T., Shimizu, H. M., Kiyonagi, Y., Kamiyama, T., Hiraga, F., Iwasa, H., Sato, K. & Furusaka, M. (2004). *Nucl. Instrum. Meth. A*, **529**, 120–124.
- Tiziani, H. J. & Uhde, H.-M. (1994). *Appl. Opt.* **33**, 567.
- Treimer, W. (2019). *Handbook of Advanced Non-destructive Evaluation*, pp. 1–85.
- Wang, X., Holden, T., Stoica, A., An, K., Skorpenske, H., Jones, A., Rennich, G. & Iverson, E. (2010). In *Mechanical Stress Evaluation by Neutrons and Synchrotron Radiation*, vol. 652 of *Materials Science Forum*, pp. 105–110. Trans Tech Publications.
- Willendrup, P., Farhi, E., Knudsen, E., Filges, U. & Lefmann, K. (2014). *J. Neutron Res.* **17**, 35–43.
- Woracek, R., Santisteban, J., Fedrigo, A. & Strobl, N. (2018). *Nucl. Inst. Meth. A*, **878**, 141–158.
- Zhang, Q., Polikarpov, M., Klimova, N., Larsen, H., Mathiesen, R., Emerich, H., Thorkildsen, G., Snigireva, I. & Snigirev, A. (2019). *J. Synchrotron Rad.* **26**, 109–118.